DESIGN AND R&D FOR THE SPring-8 UPGRADE STORAGE RING VACUUM SYSTEM*

M. Oishi†, S. Takahashi, M. Shoji, K. Tamura, Y. Taniuchi, T. Bizen, H. Ohkuma,
JASRI, Hyogo, Japan

Abstract

A new lattice design for SPring-8 upgrade project (SPring-8-II) aiming at an ultralow-emittance ring significantly affects the storage ring vacuum design as well as severe time constraints. To solve complicated boundary conditions, some design strategies are proposed, including "exclusion of in-situ baking" and "introduction of a 12-m-long integrated chamber (LIC) by welding without flange connections." In this paper, not only the vacuum system design but also the current progress in the R&D work, such as test productions of a straight section vacuum chamber and other components, are described.

INTRODUCTION

The conceptual design report (CDR) for SPring-8 upgrade project (SPring-8-II), under planning for user operation starting again in fiscal 2022, was published in November of 2014 [1]. The vacuum system for the targeted storage ring should handle some critical boundary conditions, such as miniaturization of the vacuum chamber, an increase in the number of photon absorbers, and a severe packing factor resulting from the multi-bend achromat configuration. Furthermore, the reuse of the existing tunnel brings with it the "one-year blackout" time constraint. Considering the aforementioned circumstances, a concept of a 12-m-long integrated chamber (LIC) with a welded structure was proposed to omit in-situ baking.

Recently, the main chamber material was changed from extruded aluminum alloy to stainless steel (SS) because of the advantages of technical superiority and better storage ring performance.

DESIGN STRATEGY

Baking Strategy

In-situ baking and the following non-evaporable getter (NEG) activation cannot be carried out throughout a 1.5-km-long storage ring within the blackout period. On the other hand, even if ex-situ baking was performed in advance, the exposure of the vacuum surface to air during the installation of adjacent vacuum connections, followed only by the NEG activation, would be unreasonable. Hence, we plan to establish a high-performance and reasonable procedure to realize an ultrahigh vacuum (UHV) system in the tunnel within a limited period of time by completing the baking and NEG activation of the 12-m-LIC offline before the blackout, followed by transportation and installation in the ring tunnel while maintaining the UHV.

Pumping Strategy

Utilizing the strategy of not conducting in-situ baking, we must also give up distributed pumping by NEG coating on the main vacuum chambers because it would take an unacceptable amount of time to remove the chambers from the tunnel, reactivate them offline, and reinstall them when necessary after restarting operations, at a significantly large facility such as SPring-8. Therefore, vacuum pumping will be mainly provided by conventional discrete NEG cartridges integrated into the conflat (CF) flange. We will locally arrange the NEG pumps, some of which combine with a sputter ion pump (SIP) for the evacuation of methane and noble gases at the photon absorbers close to where the outgassing is concentrated.

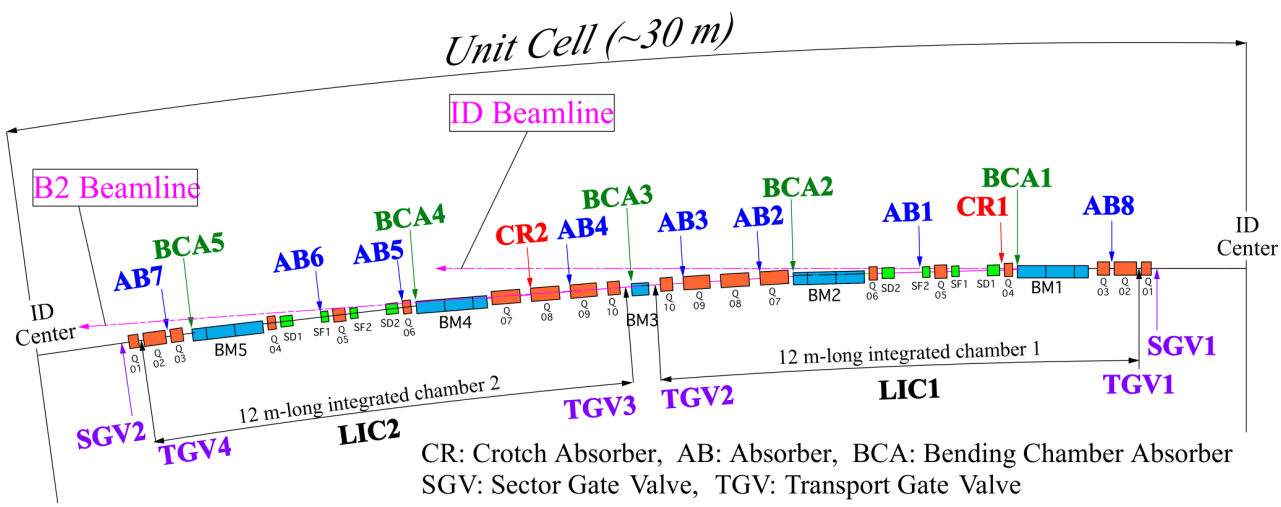

Figure 1: Schematic layout of the vacuum components for a unit cell.

ISBN 978-3-95450-147-2

VACUUM SYSTEM

Figure 1 shows the schematic layout of vacuum components for a unit cell separated by two sector gate valves (SGVs). It will be roughly divided into two sections, each of which has the LIC with two transport gate valves (TGVs) at both ends. The LICs will be moved under UHV to the tunnel and aligned inside magnets. The remaining three short connection chambers will be attached to the LICs through the TGVs. After all the connections are completed in the tunnel, the connection chambers will be baked in-situ as necessary. Then by opening the TGVs, the total vacuum system for a unit cell will be ready without exposing the vacuum surface to the atmosphere.

The total radiation power from the bending magnets is 297.9 kW (6.77 kW per unit cell), all of which, except that going to the photon beamlines, will be handled by only three types of discrete photon absorbers. As shown in Fig. 1, a unit cell has two crotch absorbers (CRs), eight absorbers (ABs), and five bending-chamber-absorbers (BCAs). The CRs and ABs are positioned between the multi-pole magnets, such that unwanted radiation will not irradiate the vacuum chamber walls. The difference between a CR and an AB is the presence or absence of a light extraction window.

Vacuum Chambers

At the stage of the CDR, the chamber was to be made from extruded aluminum alloy proven in the existing storage ring. However, we decided to change the material to SS because of the following reasons.

1. Elimination of aluminum-SS transition space.
2. High mechanical strength resulting in a reduced chamber thickness.
3. Suppression of the electron beam vibration originating from vibrations of the chamber.
4. Low outgassing rate resulting in an increase in intervals between the NEG reactivation.

Fig. 2 shows the cross-sectional drawing of a straight section vacuum chamber. The height of the slot varies from 4 mm to 9 mm, corresponding to the magnetic pole dimension and the vertical spread of synchrotron radiation. In order to increase the vacuum conductance, the height of the antechamber was enlarged within a range not interfering with the magnets.

Photon Absorbers

The photon absorbers are going to be manufactured using Glidcop or oxygen free copper (OFC) as the situation demands based on the FEM analysis result. OFC will be used when the maximum temperature does not exceed 200°C and the maximum equivalent stress does not exceed the yield point. If either of these conditions is not met, Glidcop will be used instead.

Although the heat load on each photon absorber is smaller than the existing loads at SPring-8, a compact cooling design is indispensable owing to the limited space. The double tubing configuration will be applied for miniaturization in anticipation of the jet-flow effect caused by the inner tube. Currently, we conduct a test for estimating the enhancement of the heat transfer coefficient in the jet-flow area by consolidating the results of irradiation tests and analyses, such that the design of the double tubing configuration can be optimized.

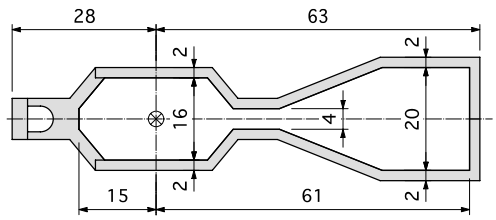

Figure 2: Cross-sectional drawing of a straight section chamber with a beam chamber of 16 mm × 30 mm.

Transport Gate Valves

The TGVs seal the LIC and maintain UHV during baking, transportation, and installation. Once the installation is completed, the TGVs are opened manually and probably never closed again except in the case of a serious vacuum problem with vacuum maintenance. The target of the face-to-face installation dimension is set at less than 50 mm with CF4$^1/_2$ flanges. A prototype, which can retain the vacuum tightness at the seat even after baking at 150°C with the seat closed, has been developed.

Pressure Calculation

The outgassing rate based on the photon stimulated desorption (PSD) is highly important in pressure calculation. The yield coefficient (η) depends on the material and accumulated photon dose. We estimated η of SS based on the literature [2] for a low beam dose and aluminum data obtained at SPring-8 for a high beam dose because we considered η to be constant irrespective of the metallic material at the high beam dose. Table 1 shows η for AB5 used in the pressure calculation, as an example.

Table 1: Yield coefficient (η) for H_2 and CO used for AB5 in the pressure calculation.

Beam dose (A·h)	η for H_2	η for CO
20	2.4×10^{-5}	3.5×10^{-6}
100	1.1×10^{-5}	1.4×10^{-6}
400	5.5×10^{-6}	6.0×10^{-7}

On the other hand,the outgassing rate based on the thermal desorption was set at constant values of 2.8×10^{-9} and 7.0×10^{-10} Pa·m^3/s/m^2 for H_2 and CO, respectively, regardless of the accumulated beam dose. The pressure distribution was calculated under the condition that a combination of the NEG and SIP were arranged at all the discrete photon absorbers where the PSD should be excited. The pumping speeds of the NEG for H_2 and CO were set at 180 l/s and 60 l/s, respectively, whereas that of the SIP for CH_4 was at 15 l/s and 6 l/s for CR/AB and BCA, respectively. Fig. 3 shows the expected total pressure distributions in a unit cell at accumulated beam doses of 20, 100, and 400 A·h. The pressure distribution for the

case of the aluminum chamber at a beam dose of 20 A·h, which is about five times higher than that of SS, is also shown. As a result, at a beam dose of 400 A·h, the gas scattering lifetime would reach 29 h. Assuming the Touschek lifetime to be 12 h, the beam lifetime is expected to be 9 h.

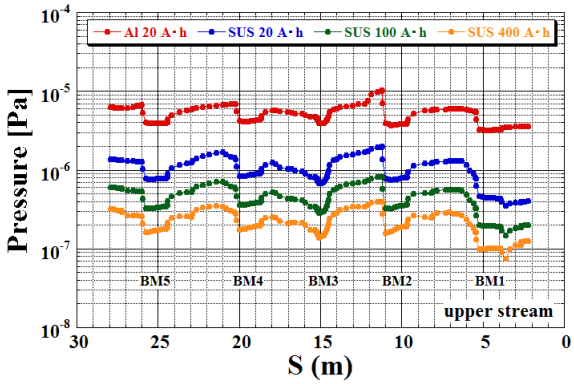

Figure 3: Expected total pressure distribution in a unit cell, excluding ID section at various accumulated beam doses.

TEST PRODUCTION

Stainless Steel Chamber

A test production of the straight section chamber was executed to establish appropriate manufacturing processes while focusing on the accuracy of the dimensions and magnetic permeability. The chamber roughly consists of a vacuum part and a cooling channel part. The former, separated in a half-divided shape, is manufactured using a roll forming method with a 2-mm-thick SS plate, and the latter using a cold drawing method, as shown in Fig. 4. After electropolishing, the inner top and bottom surfaces of the beam chamber are plated with copper with a thickness of more than 100 μm for measures to reduce the impedance. All the components are connected in a sequence using laser beam welding (LBW), having a small amount of heat input resulting in the suppression of cross-sectional deformation and bending. After welding, they were subjected to chemical polishing treatment to remove contamination, followed by vacuum annealing at more than 900°C to reduce the magnetic permeability and the outgassing rate.

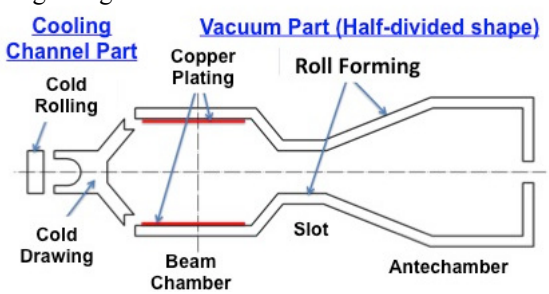

Figure 4: Vacuum chamber components, all of which are connected using laser beam welding.

A high manufacturing accuracy of the vacuum chamber is required because the clearance of the vacuum chamber and the magnetic pole is extremely narrow. We set the accuracy of the welded chamber to less than half of the manufacturing tolerance for an extruded aluminum chamber specified by the Japanese Industrial Standards. Dimension measuring apparatus with high accuracy, such as High-speed 3D Laser Scanner (LJ-V) manufactured by KEYENCE Corporation, was employed to estimate the manufacturing accuracy of the cross-sectional deformation, bending, and twisting. It was confirmed that bending in the horizontal direction, occurring in the LBW process, could be suppressed to less than 1.8 mm/2 m by heat-straightening using the laser beam of the LBW device. Although a little twisting and bending in the vertical direction were detected, they could be corrected during the installation into the magnets because of a low cross-sectional rigidity of the chamber. The cross-sectional deformation was confirmed to be within the design accuracy. We also found that the magnetic permeability could be reduced by vacuum annealing to an acceptable level of less than 1.03 in the vicinity of the beam chamber.

RF Finger for Bellows

We ran a trial manufacture for two types of RF fingers for bellows in order to design an appropriate configuration that can be inserted in a narrow space owing to the limited packing factor. Type A (Fig. 5(a)), made of beryllium copper with a thickness of 0.1 mm, 0.2 mm, and 0.3 mm, has the same structure as the one in use at SPring-8. Type B (Fig. 5(b)), which is prepared for the bellows whose length is reduced to minimum, is equipped with an additional part called a spring finger that presses the RF finger such that the RF finger does not separate from the chamber. The spring finger is made of silver-plated inconel with a thickness of 0.2 mm. Both types have a part that restricts excess expansion of the bellows and prevents the RF finger from dropping. As a result of repeated movement tests applied in the axial, right-angled, and angular directions, any presence of a gap between the finger and chamber or a break in the finger was not detected for both types. A 0.2-mm-thick finger is the best for Type A. As for Type B, because the contact load between the spring finger and the RF finger was twice the design value, reconsideration of the configuration of the spring finger would be necessary.

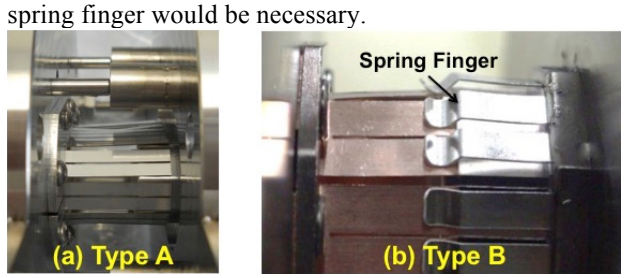

Figure 5: Test production of the RF finger for the bellows, (a) Type A and (b) Type B .

REFERENCES

[1] SPring-8-II Conceptual Design Report, http://rsc.riken.jp/pdf/SPring-8-II.pdf

[2] Mathewson et al., AIP Conf. Proc. 236, 313 (1991).

ISBN 978-3-95450-147-2